Linearized wave-equation migration velocity analysis by image warping

Francesco Perrone[1], Paul Sava[1], Clara Andreoletti[2], and Nicola Bienati[2]
[1] *Center for Wave Phenomena, Colorado School of Mines*
[2] *eni E&P*

ABSTRACT
Seismic imaging by wavefield extrapolation aims to produce images of contrasts in physical parameters in the subsurface, e.g., velocity or impedance. In order to build such images, a background model describing the wave kinematics in the Earth is necessary. In practice, both the structural image and the background velocity model are unknown and have to be estimated from the acquired data. Migration velocity analysis deals with estimation of the background velocity model in the framework of seismic migration and relies on two main elements: the data redundancy and the invariance of the structures with respect to different seismic experiments. Since all the experiments probe the same model, the reflectors must be invariant in suitable domains (e.g., shots or reflection angle); the semblance principle is the conventional tool used to evaluate the invariance of ta set of images. Here, we present a velocity error measure that is based on the semblance principle in the shot-domain. This measure is purely kinematic and considers the angle between the structural dip (estimated from the migrated image), and the displacement vector field, which is estimated from images obtained from shots. The maximum constructive interference, i.e., the maximum semblance, requires that the two images superimpose along the reflector slope. If the two images are not *in phase* along the reflector, then the velocity model is incorrect, and we can measure this discrepancy by estimating the angle between the dip of the reflector and displacement vector field. We derive an expression for the image perturbation that drives a migration velocity analysis procedure based on a linearization of the wave-equation with respect to the model parameters; we then compare our method with the direct implementation of the based on the difference of images from nearby experiments. The two approaches lead to similar optimization problems. For nearby shots, the image difference has the characteristics of an image perturbation and is robust against cycle skipping. It, however, is sensitive to amplitude patterns and even for the correct velocity model it can produce nonzero velocity updates. Synthetic 2D examples show promising results in retrieving macro velocity models. This methodology can be directly applied to 3D.

Key words: tomography, migration velocity analysis, imaging

1 INTRODUCTION

Seismic imaging aims to construct an image of geologic structures in the subsurface from reflection data recorded at the surface of the Earth. For constructing such an image, one needs the Green functions that describe the wave propagation in the subsurface and hence a model for computing the Green functions. If we assume a linear, acoustic, and constant-density model, the velocity is the only parameter that governs the wave propagation. The correct velocity model is unknown and must be estimated from the data to obtain an accurate image of the reflectors in the subsurface, especially for highly heterogeneous geologic configurations. Complex wave propagation phenomena (for example, multipathing) cannot be correctly handled and the structures in the subsurface cannot be properly imaged, unless the background velocity model is accurately estimated.

Estimating the velocity model from the recorded data is referred to as *velocity analysis*. The problem is instrisically nonlinear (because the wave-equation is nonlinear in the velocity parameter) and it is usually formulated as an optimization problem in which the correct velocity model minimizes an objective function. Two different classes of methods for estimating the wave propagation velocity have been dis-

cussed in the literature: waveform inversion (WI) (Tarantola, 1984; Woodward, 1992; Pratt, 1999; Plessix, 2009) and migration velocity analysis (MVA) (Yilmaz, 2001; Sava and Biondi, 2004; Shen and Symes, 2008; Symes, 2008). WI operates in the data domain and iteratively updates the model parameters until the energy of the residual between simulated and recorded data is minimized. The WI objective function is characterized by numerous local minima and a good initial guess of the velocity model is necessary in order to converge to the correct solution. Migration velocity analysis relies on the assumption that the reflectors in the subsurface must be imaged at the same locations by different experiments. When the correct velocity model is used, the similarity between the images constructed for different experiments must be maximum. The similarity of the migrated images (i.e., the semblance principle (Al-Yahya, 1989; Symes, 2008)) constitutes the criterion for designing an objective function that measures the quality of the velocity model.

Evaluating the semblance of a set of images requires constructing common-image gathers, i.e., new images indexed in spatial position and either an extension parameter (e.g., incidence angle, space/time lags (Rickett and Sava, 2002; Sava and Fomel, 2003) or experiments (Soubaras and Gratacos, 2007; Xie and Yang, 2008)). Image gathers allow one to assess the consistency between the velocity model and the recorded data. The construction of image gathers requires the migration of the entire survey or at least of a subset of the recorded shots that illuminate the portion of the subsurface we are interested in. Consequently, in order to handle the disk storage requirements and computational cost associated with the analysis, it is necessary to subsample the locations where the gathers are constructed.

In this paper, we present a measure based on the differential semblance criterion (Symes and Carazzone, 1991) for evaluating the correctness of the velocity model in the framework of migration velocity analysis. Our method operates in the image-domain and computes the displacement vector field between two images. The displacement vector field is defined by a warping transformation of one image into the other and is pointwise measured by local crosscorrelations of the two images. The displacement vector field and the estimated structural dip give us tools for extracting a purely kinematic measure of semblance in the image domain without constructing common-image gathers (CIGs).

The motivation for the work is multifold. First, by operating on a shot-by-shot basis, we eliminate the cost associated with construction of image gathers, which requires the migration of the entire dataset or, alternatively, of the shots that illuminate the target area. Consequently, the disk storage is reduced, thus decreasing the complexity and speeding-up the actual migration velocity analysis algorithm. Second, typical CIGs constructed at fixed lateral positions capture the vertical movement of the image point as a function of the extension parameter, although an error in the velocity model can produce a movement in all directions in space. Our technique does not assume a simple vertical shift of the image point and restates the semblance principle in terms of the consistency between the structural information in the image and the apparent displacement of image points as a function of experiments. Finally, the shot-by-shot approach allows one to bootstrap the MVA procedure without recording the whole dataset; thus we can update the velocity model in an iterative fashion with respect to shots.

In the following sections, we describe the semblance principle, we review the wave-equation migration velocity analysis (WEMVA) procedure, and then we introduce our approach for measuring the consistency of the velocity model based on the apparent shift between two images from adjacent shots.

2 THE SEMBLANCE PRINCIPLE

In seismic migration, the velocity model is assumed to be known but in reality it represents the main unknown and has to be estimated from the data. Migration velocity analysis measures the similarity of the different migrated images (which are obtained by exploiting the redundancy of the data) using the semblance principle (Al-Yahya, 1989). The semblance principle relies on the invariance of the subsurface with respect to the seismic experiments: since the model that generates the data is unique and time-invariant, different experiments must image the same structures. The quality of the migration result is assessed by constructing an image cube that collects the images as a function of the spacial coordianates $\mathbf{x}$ and experiment $R(\mathbf{x}, e)$ or extension parameter $R(\mathbf{x}, \alpha)$. The variable e indexes the experiments and can represent the shot number or the ray-parameter in plane-wave migration; the extension parameter α can represent the reflection angle or the subsurface offset. The current practice consists in analyzing fixed spatial locations and considers all the experiments (Figure 1(a)) or all the values of the extension parameter (Figure 1(b)). If the velocity model is correct, the images show invariance along these dimensions in the image cube. This property is true in a kinematic sense: the reflection coefficients (Aki and Richards, 2002), which depend nonlinearly on the incidence angle, are neglected by this methodology. Several choices of domain are available for analyzing the invariance in the image cube, for example the extended image domain (Rickett and Sava, 2002; Symes, 2008; Vasconcelos, 2008), the reflection angle domain (Sava and Fomel, 2003; Biondi and Symes, 2004b), and the experiment domain (Chavent and Jacewitz, 1995; Soubaras and Gratacos, 2007; Xie and Yang, 2008).

The semblance principle can be implemented in different fashions:

(i) In conventional semblance (Taner and Koehler, 1969), the energy of the stack of the migrated images measures the quality of the velocity model; the correct velocity model maximizes that energy;

(ii) In differential semblance (Symes and Carazzone, 1991), the energy of the first derivative along the extension axis measures the correctness of the velocity model; the correct model minimizes the energy.

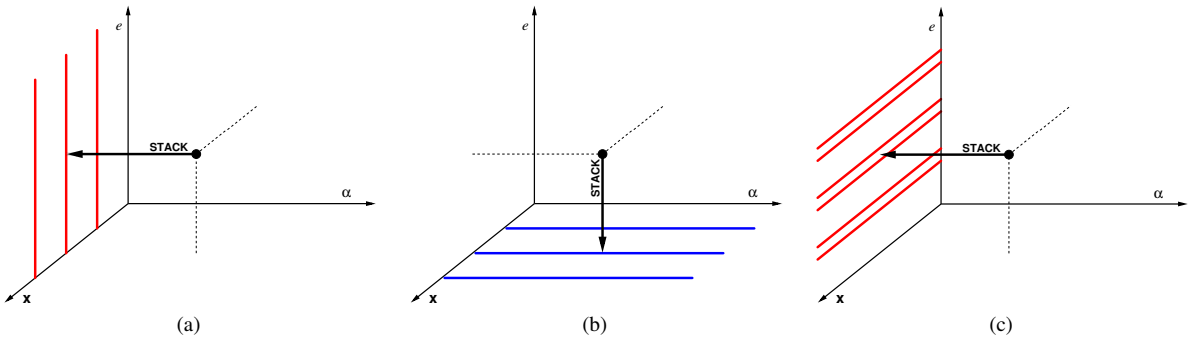

Figure 1. Migrated images can in principle be ordered in a hypercube and indexed by spatial location $\mathbf{x}$, experiment number e, and extension parameter α. By staking along one of the axes we reduce the dimensionality of the data and are able to analyze them. For example, we can stack along the extension parameter axis (e.g., reflection angle) and evaluate model accuracy by measuring the semblance at discrete positions in space between images corresponding to all experiment indices (a). Alternatively, by staking together images from all experiments, we obtain common-image gathers (e.g., angle-domain common-image gathers), which we usually analyze at fixed spatial locations (b). A third option is to stack over the extension parameter and to analyze all points in the image for two (or a small number of) images obtained from nearby experiments (c). This last solution is what we propose in this paper.

Both conventional and differential semblance are customarily implemented using gathers, e.g., common-offset or common-reflection angle, in order to analyze the consistency between different results. Inconsistency in the migrated images appears as moveout in the gathers; the moveout is used for estimating the velocity error and for computing the velocity update for the current model. If we consider common-image gathers, we have the situation depicted in Figures 1(a) and 1(b). Since differential semblance considers similarities between adjacent experiments, in principle we can work without gathers in an iterative fashion by considering pairs of experiments (Figure 1(c)). This approach allows one to analyze all the points in the aperture of the two experiments at the same time, instead of constraining the appraisal of the velocity model at specific spatial locations where the CIGs have been constructed.

In this work, we explore an alternative method for measuring semblance in the experiment domain. The experiment index may represent the shot number or the plane-wave ray-parameter, and we consider all points in the aperture shared by adjacent shot-gathers. The semblance principle is implemented in a differential sense by measuring the constructive interference of two images. This point of view has several advantages. The computational cost is reduced since we can analyze all the points in the aperture shared by two experiments at once instead of looking at particular spatial locations where the gathers are constructed. Thus, the resulting velocity update influences a wider portion of the velocity model and potentially speeds up the convergence towards a solution. Differential semblance in the experiment domain is flexible and can be implemented independent of the migration algorithm used for imaging the data. The potential disadvantages are related to the amplitude differences between the two images: two neighboring experiments are likely to supply the same structural image but with different amplitude footprint. If the velocity field that generated the data produces observable changes in amplitude between adjacent experiments (for example, because of shallow lenses), the simple difference between the corresponding images (if small but not zero) is an inaccurate measure of similarity and can lead to spurious velocity updates even if the migration velocity model is correct. We develop a measure that is not so sensitive to the amplitude patterns.

3 IMAGE WARPING AND VELOCITY MODEL INCONSISTENCY

The seismic image forms at the stationary points of the traveltime between the source and receiver position. When we stack the images from different shots, we evaluate the stationary point with respect to the shot position; specular reflectors build up along the structural slope, and the residual diffractions caused by limited aperture stack out. If the velocity model is incorrect, the stationary point at depth changes with experiment: the different images are not "in phase", and the interference is not totally constructive, thus reducing the overall amplitude of the stack. If we consider two adjacent experiments (e.g., shots), we can assess the consistency between the corresponding partial images (i.e., images obtained from single shots or plane waves) by evaluating the degree of constructive interference of the migrated events. In other words, we measure the relative displacement of two images. A conventional differential semblance approach requires the migration of the entire survey and compares pairs of adjacent images after a mapping in a suitable domain (e.g., in the angle-domain) at fixed spatial locations; our differential semblance approach compares pairs of images from adjacent experiments at every image point and measures inconsistencies as phase shifts in the image space. Because this methodology includes all points in the aperture at once, it does not require the construction of gathers. The phase shift between the two images is measured as the angle between the dip field estimated from the reflectors in the images and a second vector field that warps one image into the other.

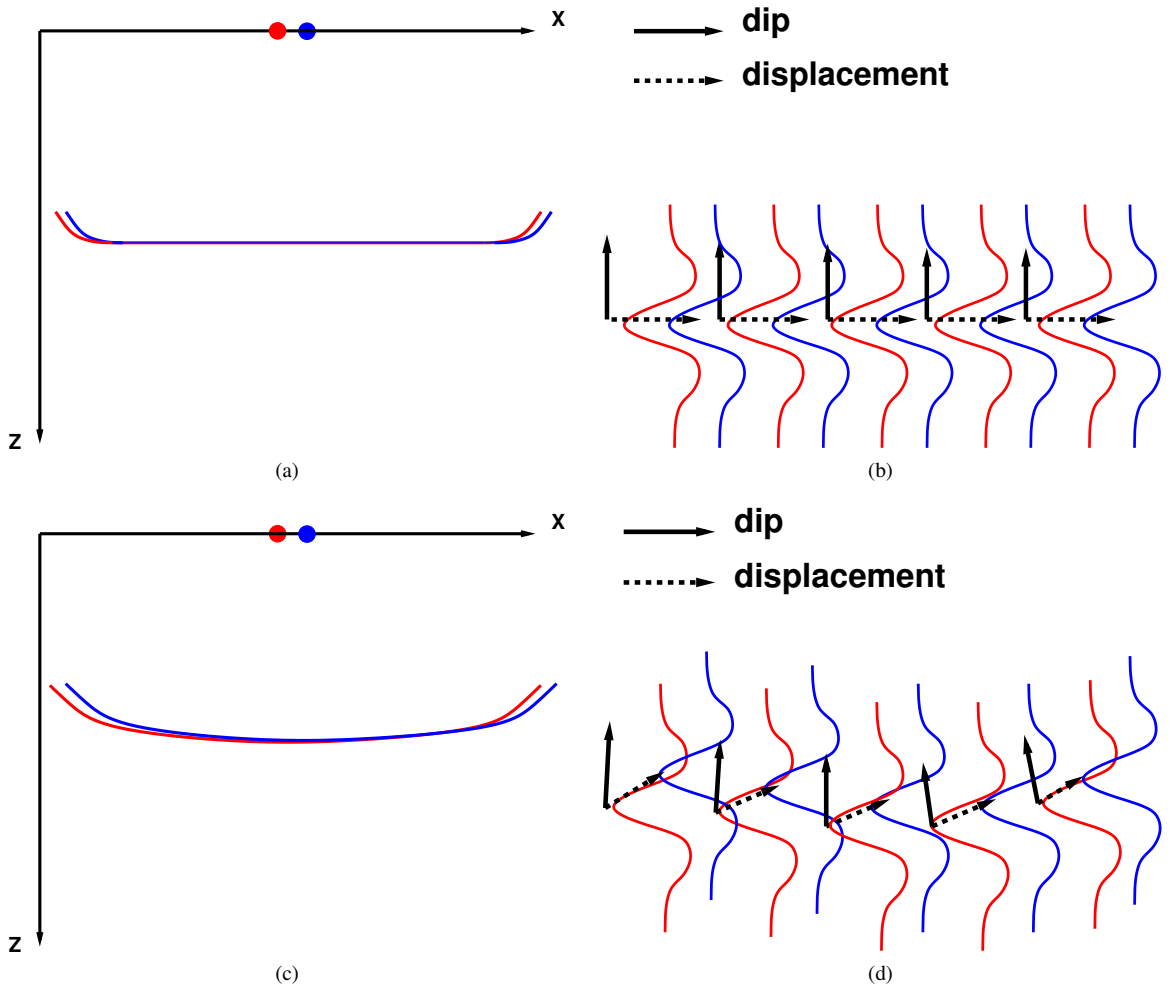

Figure 2. Horizontal reflector for correct velocity model (a); the images obtained from two adjacent shots (red and blue dot) overlap and interfere constructively in the aperture. The dip field estimated along the structure and the displacement field between the two images are perfectly aligned (b). Horizontal reflector for incorrect velocity model (c); the two images no longer perfectly overlap. The dip and displacement fields form a non-zero angle that measures the inconsistency between the two results (d).

3.1 Objective function from image warping

To measure velocity errors in the experiment-image domain, we need to design the objective function to be optimized. The objective function measures information about the model parameters supplied by the seismic experiments; this information is encoded in terms of, for example, focusing or semblance of prestack images (Symes, 2008). Given two images, we construct two vector fields: the structural dip field and the relative displacement, or warping, vector field. The first can be obtained from either of the considered images; the second links the two images and is computed considering the spatial local crosscorrelation of the two images at every point. If the velocity model is correct, images from adjacent shots feature the same structural dip (this is another expression of constructive interference), and the dip and warping fields are orthogonal (Figure 2(a) and 2(b)). In contrasts, if the velocity model is incorrect, the two vector fields are not pointwise orthogonal (Figure 2(c) and 2(d)); the stack of different experiments is not completely constructive normal to the structural dip and the wavelet in the final image loses its symmetry (in case the data are otherwise zero-phase) (de Vries and Berkhout, 1984). The angle between the dip and warping field therefore measures the quality of constructive interference between the two shots and supplies an error indicator for MVA.

The orthogonality between two vectors is measured by their inner product. The dip field can be estimated using, for example, plane-wave destruction (PWD) filters (Fomel, 2002) or gradient square tensors (van Vliet and Verbeek, 1995; Hale, 2007a) whereas the warping field is computed using spatial local crosscorrelation of the input images at every spatial location (Hale, 2007b). Figure 3 shows the dip (black arrows) and displacement vector field (white arrows) computed from the migrated images of a horizontal reflector; the velocity error is constant across the model. Note that only when the velocity

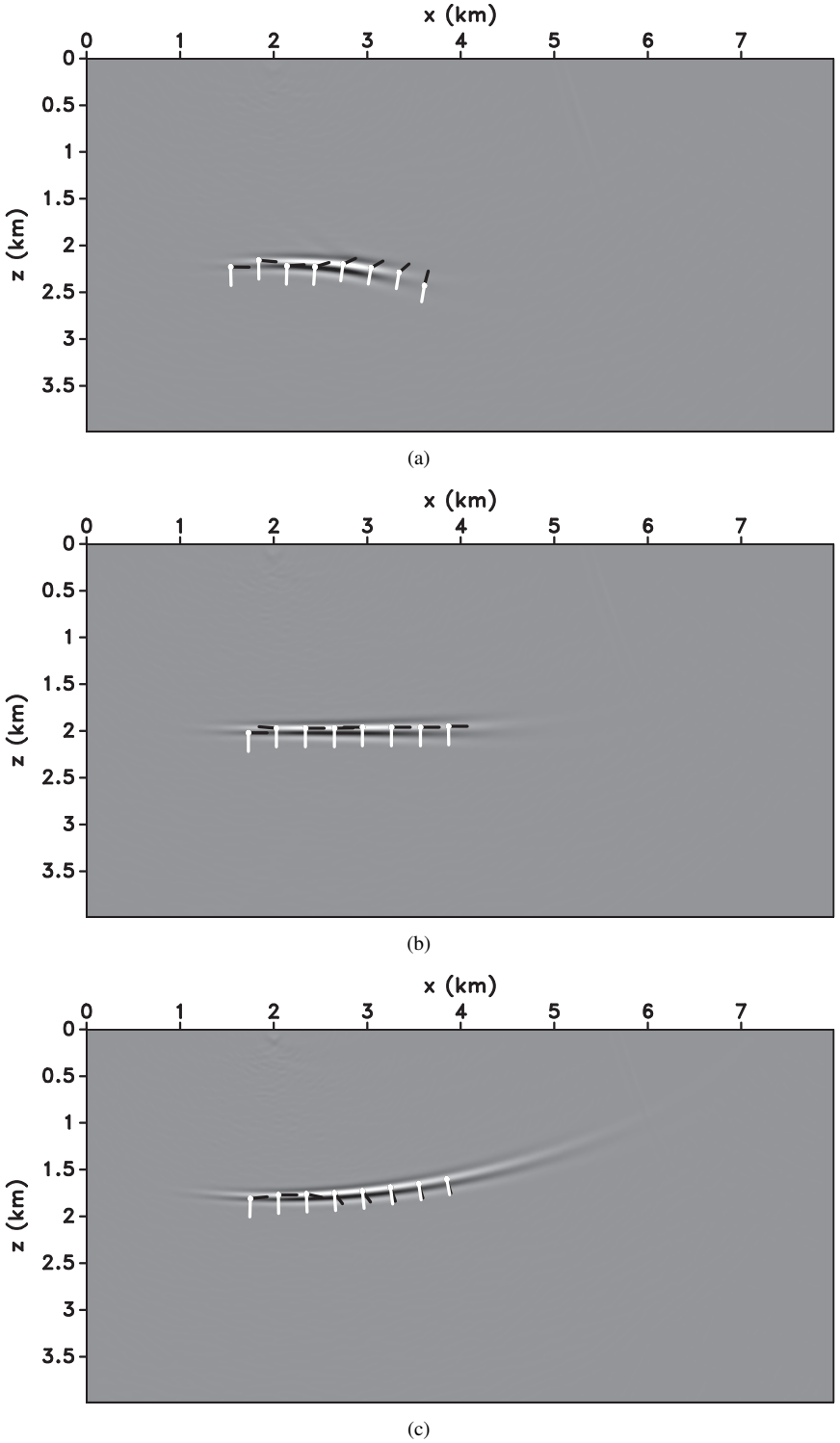

Figure 3. Horizontal density interface imaged using a single shot at $x = 2$ km and 800 receivers spaced 10 m at every grid point at the surface. The angle between the dip (white arrows) and displacement vector field (black arrows) indicates a velocity error: (a) velocity too low, (b) correct velocity, and (c) velocity too high. The displacement vector field is computed using a second image obtained from a shot located at $x = 2.05$ km.

model is correct, are the two vector fields orthogonal at every image point. In order to obtain the image and the vector fields, we migrated two shots located at $x = 2$ km and $x = 2.05$ km, the horizontal interface is due to a density contrast and the velocity model is constant. Our semblance measure can be directly extended to 3D, where the dip vector is normal to the plane tangent to the reflector at every spatial location.

The objective function we define is

$$J_{vec}(s) = \frac{1}{2}\|\mathbf{d}(\mathbf{x}) \cdot \mathbf{u}(\mathbf{x})\|^2, \tag{1}$$

where $\mathbf{d}(\mathbf{x}) = \mathbf{D}[\mathbf{x}](R_i)$ represents the dip vector field, $\mathbf{u}(\mathbf{x}) = \mathbf{U}[\mathbf{x}](R_i, R_j)$ is the warping vector field between the two images, R_i and R_j, and the inner product is computed at every image point. The operators $\mathbf{D}[\mathbf{x}]$ and $\mathbf{U}[\mathbf{x}]$ are the dip and the warping estimation operator, respectively. If the model is correct, the inner products are zero and the objective function $J_{vec}(s)$ is minimum. The two images R_i and R_j are functions of three variables themselves: the experiment index (which we denote by i and j), the position vector $\mathbf{x}$, and the model $s = s(\mathbf{x})$ we used for computing the image:

$$\begin{aligned} R_i &= R_i(\mathbf{x}, s), \\ R_j &= R_j(\mathbf{x}, s). \end{aligned}$$

We parametrize the problem using the slowness rather than velocity because the WEMVA operator is obtained by linearizing the one-way migration operator with respect to slowness (Sava and Biondi, 2004). Note that by measuring the angle between the dip and warping vector fields, we obtain an objective function (equation 1) that is insensitive to amplitude variation as a function of experiment. This feature is particularly helpful because amplitude is a second-order effect with respect to velocity. The warping vector field that maps one image into the other absorbs the amplitude pattern information and makes the approach robust against differences in illumination, geometrical spreading, and reflection coefficient.

In the next section, we show that the objective function obtained from the warping and the dip vector field is equivalent to the formulation of differential semblance in the experiment-image domain when we consider pairs of adjacent experiments in the limit of small separation between them (e.g., adjacent shots or plane waves with similar ray-parameter).

3.2 Image difference and image warping

In this section, we link the objective function in reqobjFunVec to the energy of the image difference using the warping relationship that locally relates two images. The difference operator is a linear operator, and the established link gives us the handle to construct a WEMVA operator and set up the velocity analysis problem as a sequence of linearized inverse problems.

The gradient operator $\nabla = (\frac{\partial}{\partial x}, \frac{\partial}{\partial y}, \frac{\partial}{\partial z})^T$ applied to the image returns the vector that points toward the maximum increase. It operates as an edge detector and supplies the direction normal to the reflector. Because of the oscillating nature of the signal, the orientation of the gradient vector changes by 180 degrees across the wavelet. Nonetheless, since we are interested in the orthogonality between the dip and warping vector fields, we typically consider the gradient of the image instead of the dip field without loss of information. Hence, we can rewrite equation 1 as

$$J_{vec}(s) = \frac{1}{2}\|\nabla R_i(\mathbf{x}, s) \cdot \mathbf{u}(\mathbf{x})\|^2. \tag{2}$$

The warping field between two neighboring images is estimated assuming that locally

$$R_j(\mathbf{x}, s) = R_i(\mathbf{x} + \mathbf{u}(\mathbf{x}), s). \tag{3}$$

If we also assume that the warping vector $\mathbf{u}(\mathbf{x})$ is small in that the two experiments illuminate the same portion of the subsurface, we can rewrite equation 3 using a Taylor series expansion as

$$R_j(\mathbf{x}, s) \approx R_i(\mathbf{x}, s) + \nabla R_i(\mathbf{x}, s) \cdot \mathbf{u}(\mathbf{x}). \tag{4}$$

Equation 4 allows us to approximate the image difference $R_j(\mathbf{x}, \mathbf{v}) - R_i(\mathbf{x}, \mathbf{v})$ as

$$R_j(\mathbf{x}, s) - R_i(\mathbf{x}, s) \approx \nabla R_i(\mathbf{x}, s) \cdot \mathbf{u}(\mathbf{x}). \tag{5}$$

We can now invoke the semblance principle: if the model is correct, the image difference for neighboring experiments must be minimized. Considering equation 5 and computing the energy of $R_j(\mathbf{x}, s) - R_i(\mathbf{x}, s)$, we obtain

$$J_{diff}(s) = \frac{1}{2}\|R_j(\mathbf{x}, s) - R_i(\mathbf{x}, s)\|^2 \approx \frac{1}{2}\|\nabla R_i(\mathbf{x}, s) \cdot \mathbf{u}(\mathbf{x})\|^2, \tag{6}$$

which is exactly equation 2.

These results hold as long as the two experiments actually illuminate the subsurface in the same aperture. The inner product between the dip and warping field relies on the assumption of specular reflectors, whose dip varies slowly across the image; the constructive interference between different experiments within the aperture ensures that the minimum of the objective function is zero for all practical purposes. We use equation 5 to construct the wave-equation migration velocity analysis operator (Biondi and Sava, 1999; Sava and Biondi, 2004) for our objective function (equation 1).

3.3 Wave-Equation Migration Velocity Analysis

In this section, we derive the expression for the wave-equation migration velocity analysis (WEMVA) operator (Biondi and Sava, 1999; Sava and Biondi, 2004) for our objective function (equation 1). A detailed presentation of the WEMVA procedure can be found in Sava and Biondi (2004); implementation aspects are described by Sava and Vlad (2008).

The WEMVA operator is based on a linearization of the extrapolator operator and the single-scattering (Born) approximation. The main goal of this method is to link a perturbation Δs in the slowness field with the perturbation ΔR in the image that is obtained after migration. Because of the linearization, the link is described by a linear operator.

The image $R(s)$ depends on the slowness model s through the source and receiver wavefields $W_S(s, \omega)$ and

$W_R(s,\omega)$

$$R(s) = \sum_{\omega} \overline{W}_S(s,\omega) W_R(s,\omega), \tag{7}$$

where the overline indicates the complex conjugate operator and ω represents the temporal frequency. The wavefields are constructed in the frequency domain using a one-way phase-shift operator (Sava and Vlad, 2008). In equation 7, the image $R(s)$ depends nonlinearly on the model s; the nonlinearity comes from the wave-equation, which we have to solve for computing the source and receiver wavefields $W_S(s,\omega)$ and $W_R(s,\omega)$.

To linearize the relationship between the image and model, we assume a "small" perturbation Δs that would produce small perturbations in the wavefields. In the following, we drop the dependence on ω and s for the sake of readability. By perturbing equation 7 with respect to the slowness field, we obtain

$$R + \Delta R \approx \sum_{\omega} \left(\overline{W}_S W_R + \overline{\Delta W}_S W_R + \overline{W}_S \Delta W_R \right), \tag{8}$$

where ΔW_S and ΔW_R are the linear perturbations in the source and receiver wavefields resulting from a perturbation Δs in the slowness model. ΔR represents the perturbation that would be observed in the image.

Using equation 8, we can relate the image perturbation ΔR and the wavefield perturbation by removing the background image from the left and right side of the equation to obtain

$$\begin{aligned} \Delta R &\approx \sum_{\omega} \left(\overline{\Delta W}_S W_R + \overline{W}_S \Delta W_R \right) \\ &\approx \mathbf{L} \Delta s. \end{aligned} \tag{9}$$

In equation 9, the wavefield perturbations $\Delta W_S = \Delta W_S(\Delta s)$ and $\Delta W_R = \Delta W_R(\Delta s)$ depend linearly (Born approximation) on the slowness perturbation Δs (Sava and Vlad, 2008). Thus the image perturbation ΔR is obtained by applying a linear operator $\mathbf{L}$ to the model perturbation Δs (Sava and Biondi, 2004).

This result is the basis for the derivation of the WEMVA operator for our objective function. Let us consider two shots and build the image perturbation for the individual shots and their difference for a certain model perturbation Δs:

$$\begin{aligned} \Delta R_i &= \mathbf{L}_i \Delta s \\ \Delta R_j &= \mathbf{L}_j \Delta s \\ \Delta R_j - \Delta R_i &= (\mathbf{L}_j - \mathbf{L}_i) \Delta s; \end{aligned} \tag{10}$$

the operators $\mathbf{L}_i$ and $\mathbf{L}_j$ differ because they are constructed using wavefields from the two experiments i and j, even though they use the same background model. Equation 10 shows that we can linearly combine the WEMVA operator to obtain the image perturbation for a linear combination of a set of images. This result follows from the linearity of the operator itself. Before assuming that equation 10 is the definition of the WEMVA operator for our objective function, we need to show that the right-hand side does represent an image perturbation. Let us consider two images $R_i = R_i^c + \Delta R_i$ and $R_j = R_j^c + \Delta R_j$. Each of them is the superposition of the image in the background correct model (R_i^c and R_j^c) and the image perturbation caused by the model perturbation Δs (ΔR_i and ΔR_j); then the difference of the two images is

$$R_j(\mathbf{x}) - R_i(\mathbf{x}) = R_j^c(\mathbf{x}) - R_i^c(\mathbf{x}) + \Delta R_j - \Delta R_i. \tag{11}$$

If the shots are close enough, the similarity of the images obtained in the correct background model is maximum, and their difference in equation 11 goes to zero:

$$R_j(\mathbf{x}) - R_i(\mathbf{x}) \approx \Delta R_j - \Delta R_i. \tag{12}$$

Equation 12 shows that under the assumption of small separation between the shots, the image difference $R_j(\mathbf{x}) - R_i(\mathbf{x})$ gives us an approximation of the image perturbation we need for the WEMVA operator.

3.4 Image perturbation

The formulation of the optimization problem for velocity analysis discussed in the preceding sections gives a handle for constructing an image perturbation that drives the velocity update in wave-equation migration velocity analysis (WEMVA) (Biondi and Sava, 1999; Sava and Biondi, 2004). As previously discussed, an objective function based on the image difference is potentially sensitive to differences in amplitudes, for example because of the presence of strong shallow lenses. A model update attributable only to amplitude differences is a serious drawback that we want to avoid.

Again, the objective function based on the dip (gradient) and warping vector fields is purely kinematic: the measure of orthogonality between the two fields, i.e., the measure of constructive interference between the data for the two shots, exploits amplitudes in the images but it is not biased by them. Moreover, it automatically leads to an image perturbation ΔR that is asymptotically equivalent to the image difference. Consider again the two images R_i and R_j and assume that they are related by the expression in equation 3. By linearizing equation 3, we obtained the relationship between the difference of the images and the product of the gradient of the image and the displacement field. We can thus consider the first-order term of equation 4,

$$\Delta R = \nabla R_i(\mathbf{x}, s) \cdot \mathbf{u}(\mathbf{x}), \tag{13}$$

as the image perturbation for WEMVA. Since the gradient of the image is parallel to the dip vector when the model is correct, the image perturbation ΔR in equation 13 is zero for all practical purposes (whereas the image difference is not), and we avoid a velocity update driven only by differences in the amplitudes between the two images.

4 NUMERICAL EXAMPLES

We next present a few numerical examples to describe our methodology. First, we show the behavior of the objective function for a simple model. Second, we show the computed

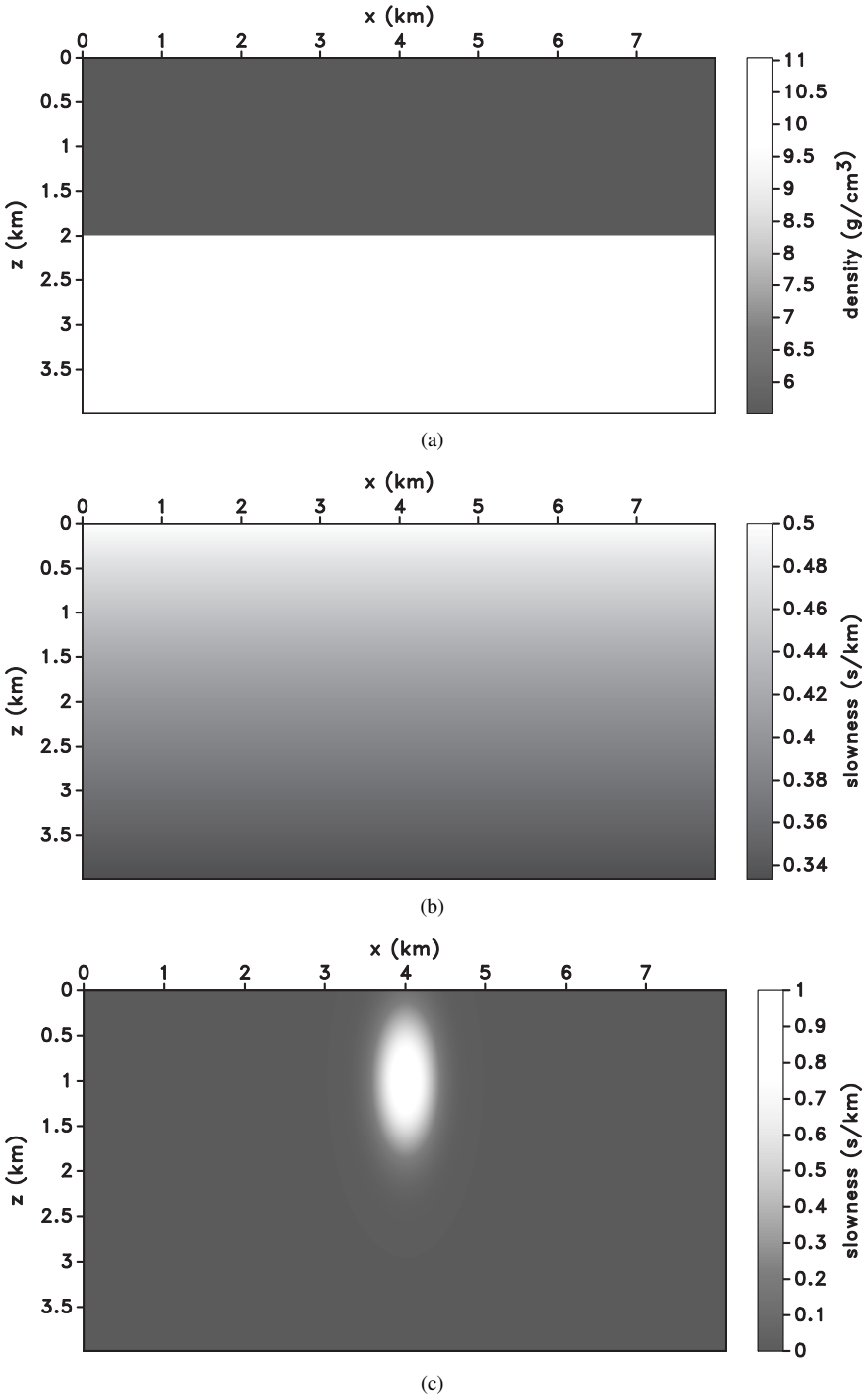

Figure 4. Vertical section of a 3D model with azimuthal symmetry. (a) Density model, (b) background slowness model, and (c) slowness anomaly.

image perturbations and backprojections using the adjoint WEMVA operator. The first inversion test considers a simple model with a stack of horizontal density interfaces in a vertical velocity gradient; we perturb the slowness model with two Gaussian anomalies with opposite sign, run 10 iterations of nonlinear conjugate gradient, and correct the model. We conclude the section showing the inversion results obtained on the marmousi dataset using a very limited number of shot-gathers. Our methodology is able to correct the model and obtain a more geologically plausible image.

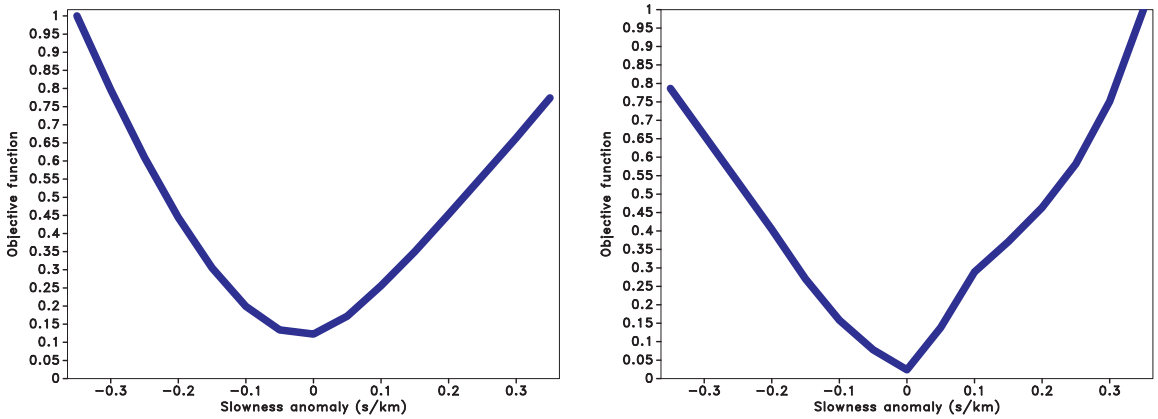

(a) (b)

Figure 5. 2D sensitivity test. Objective functions computed from (a) the image difference and (b) the inner product of dip and displacement vector fields for the model presented in Figure 4

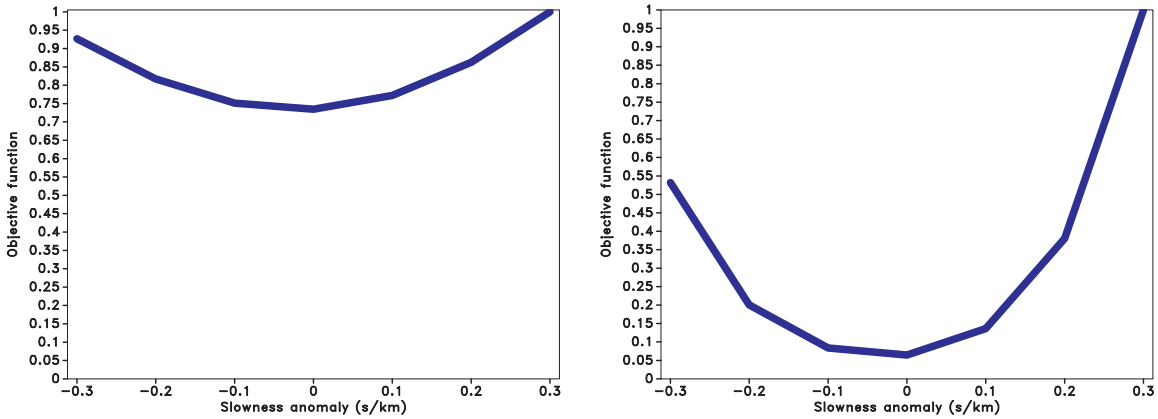

(a) (b)

Figure 6. 3D sensitivity test. Objective functions computed for (a) image difference and (b) inner product of dip and displacement vector fields in the 3D extension of the model in Figure 4. Note that the warping approach leads to a steeper objective function.

4.1 Objective functions

Consider a horizontal reflector in a 3D model with a vertical slowness gradient (Figure 4(a) and 4(b)). The interface is a density contrast, and the data are modeled with a two-way finite-difference algorithm. We contaminate the data with Gaussian random noise; the signal-to-noise ratio for each shot-gather is fixed and equal to 10. We first consider a 2D slice of the model and run a 2D sensitivity test. We migrate the data with a downward continuation operator (Stoffa et al., 1990) and different amplitudes of the velocity anomaly in Figure 4(c). We migrated two shots located at $x = 2$ km and $x = 2.05$ km changing the value of the anomaly in the model to perform a sensitivity analysis. Figure 5 shows the computed objective functions from the image difference (5(a)) and image warping approach (5(b)). Both measures lead to smooth and monomodal objective functions in a wide range of realistic velocity errors (from -0.4 km/s to 0.5 km/s peak amplitude). The similarity between the behavior of the two objective functions supports our claim that the two approaches are actually connected for finite shot separation, as shown in the previous sections. Nonetheless, the minimum value of image difference objective function is not zero (Figure 5(a)) because of the different amplitude pattern in the two images. In the 3D case with the azimuthally symmetric anomaly in Figure 4(c), our image warping approach produces a distinctly steeper objective function (Figure 6), which implies more sensitivity to velocity errors. The image difference approach (6(a)) produces a strong nonzero value for the correct model in the objective function compared with the warping approach (Figure 6(b)). Moreover, the objective function for the image difference is much less sensitive to velocity errors. We observed that this problem is mainly due to the healing of the wavefield below the anomaly that produces a fairly continuos reflector even for incorrect models. The healing of the wavefield is more prominent in 3D than in 2D.

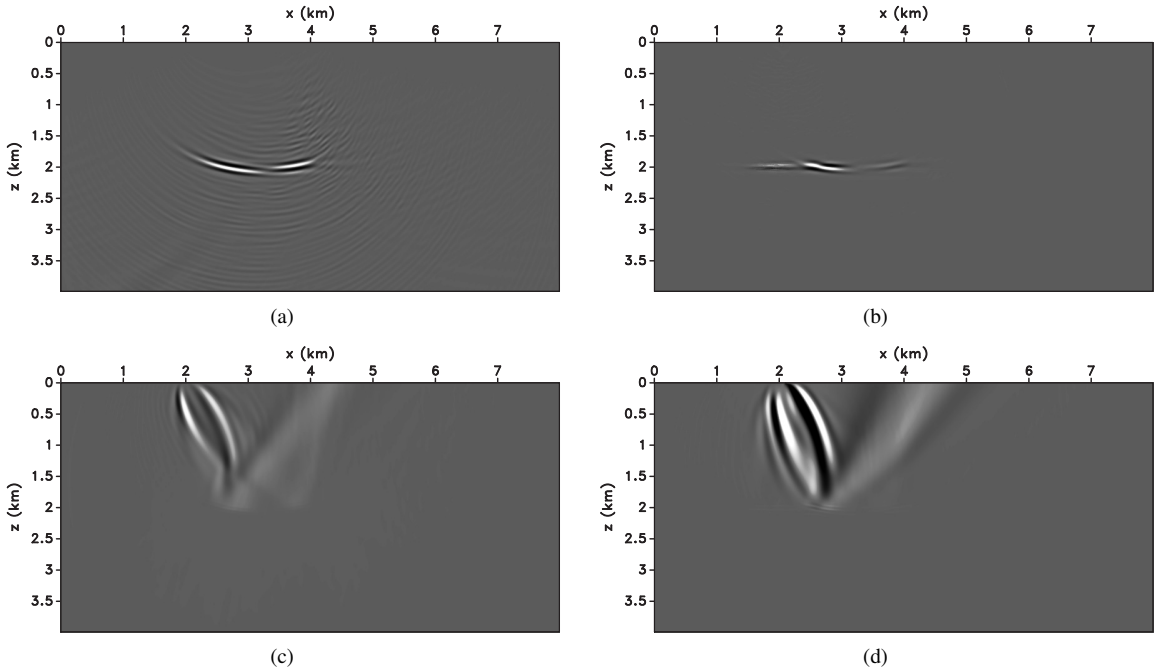

Figure 7. Image perturbations for a negative slowness anomaly computed from (a) the exact image perturbation obtained from the forward WEMVA operator and (b) image warping. Associated backprojections computed from (c) the exact image perturbation obtained from the forward WEMVA operator and (d) image warping. The phase of the wavelet of the estimated image perturbation is consistent with the ideal case, and the sign of the backprojection matches the sign of the anomaly.

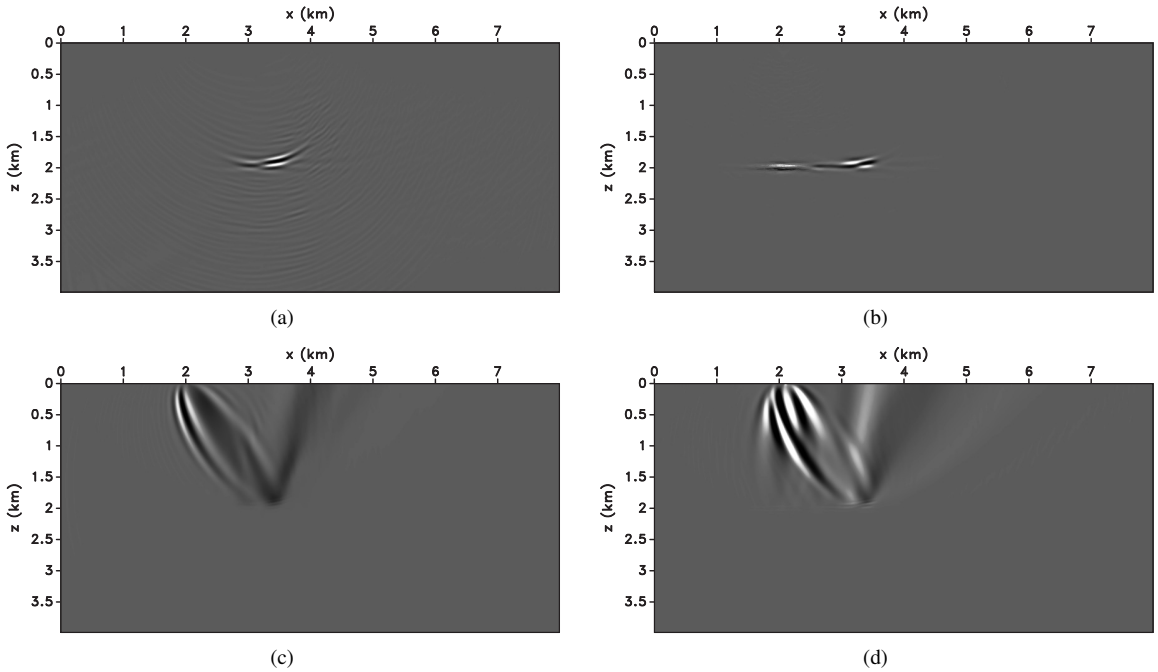

Figure 8. Image perturbations for a positive slowness anomaly computed from (a) the exact image perturbation obtained from the forward WEMVA operator and (b) image warping. Associated backprojections computed from (c) the exact image perturbation obtained from the forward WEMVA operator and (d) image warping. The phase of the wavelet of the estimated image perturbation is consistent with the ideal case, and the sign of the backprojection matches the sign of the anomaly.

4.2 Image perturbations and backprojections

The information about the model error is mainly in the phase of the image perturbation. To assess the quality of the image perturbation we obtain from the migrated images, we compare the ideal image perturbation, obtained from the direct WEMVA operator for a given slowness perturbation Δs, with the image perturbation obtained from the warping vector field. The image perturbation represents the data of a linear system of equations that link the model perturbation Δs to the image perturbation ΔR via a linear operator $\mathbf{L}$. The adjoint of the operator $\mathbf{L}$ maps the input data back in the model space and gives a scaled version of the model perturbation Δs.

Figure 7 and Figure 8 show the image perturbations and the associated backprojections computed directly from the WEMVA operator and using our image warping approach; we show two cases using a single horizontal reflector and gaussian slowness anomalies of different sign. We want to validate our procedure showing that the image perturbations and the associated backprojections we compute are consistent with the ideal case.

Figure 7(a) and 7(c) show the image perturbation that a slowness perturbation produces and the relative backprojection, which is obtained by applying the adjoint WEMVA operator to the image perturbation. They represent the ideal result since in real scenarios we do not have access to the model perturbation (which we want to estimate). In a realistic situation, we estimate the image perturbation and backproject it to estimate the slowness anomaly responsible for it. Figure 7(b) shows the estimate obtained using the image warping relation between neighboring images; by applying the adjoint of the WEMVA operator to this image, we obtain the backprojection in Figure 7(d). Observe the consistency with the backprojection in Figure 7(c). Figure 8 shows the case for a model anomaly with opposite sign. Observe that the backprojection changes sign accordingly. Note that our estimate of the image perturbation leads to a backprojection that is consistent with the ideal case scenario in which we actually know the model perturbation.

The backprojection of the estimated image perturbation contains sidelobes, which have been observed in other migration velocity analysis algorithms (Fei and Williamson, 2010); we conjecture that these artifacts are attributable to the actual nonlinearity of the estimated image perturbation in terms of the model parameters (slowness in this case).

4.3 Inversion test

As mentioned before, the estimation of model parameters for wave phenomena is a nonlinear problem because the wave-equation is nonlinear in the model parameters (slowness, density, etc.). In order to test our inversion methodology, we use a standard implementation of the nonlinear conjugate gradient algorithm (Vogel, 2002), in which the nonlinear problem is first linearized and an approximate solution is obtained. The approximate solution is then used to obtain a new linearization and then a new approximate solution, and so on. For every nonlinear iteration, we recompute the images and solve a linearized problem assuming the new background medium. The model for the inversion is shown in Figure 9: the reflectors arise from density constrasts (Figure 9(a)) and the correct slowness model is a simple vertical gradient (Figure 9(b)). We consider 24 pairs of shots at the surface; the receiver are evenly spaced by 10 m at each grid point at the surface. The shots in each pair are 50 apart and the spacing between the pairs is 250 meters; the shot pairs do not overlap.

The initial and updated velocity model are shown in Figure 10. The data for the inversion test are computed through full-acoustic (i.e., non-Born) time-domain finite-difference modeling and Gaussian random noise is added to each shot-gather separately. The signal-to-noise ratio is equal to 10. Absorbing boundary conditions are implemented to avoid surface-related multiples; the internal multiples generated by the reflectors in the model are not subtracted from the data and constitute additional source of noise.

We run 10 nonlinear iterations involving five conjugate-gradient iterations for each linearized step. The Gaussian-shape anomalies in Figure 10(a) are smoothed out by the migration velocity analysis procedure (Figure 10(b)). Figure 11 shows the resulting migrated images for the initial velocity model (Figure 11(a)) and that after five iterations of the nonlinear conjugate gradient (Figure 11(b)). Observe the improved focusing of the image, especially for the deepest reflectors.

In the examples, the absolute value of the peak of the velocity anomaly is 200 m/s, which is 10% of the minimum value of the background velocity gradient. Nonetheless, the shape of the velocity anomaly causes severe focusing/defocusing of the wavefield (depending on the sign of the anomaly), which makes migration velocity analysis challenging, especially in the initial steps. Figure 12 shows the decrease of the objective function with the number of iterations. The nonzero value of the objective function results from a number of factors: the random noise in the data, internal multiples, and the size of the local window used to compute the dip and displacement field; all of them constrain the accuracy, resolution, and sensitivity we can achieve.

4.4 Marmousi

In this section, we consider a more complex synthetic example. Figure 13 shows the correct macro velocity model for the Marmousi dataset and the anomaly used in the inversion test. We want to show the ability of our method of recovering model perturbation using a limited number of experiments (shots in this case); we consider 12 shots, evenly spaced by 0.04 km at the surface; the first shot is positioned at $x = 0.96$ km. The receivers are are spaced 0.008 km on the surface and they are located at every grid point.

We perturb the model in Figure 13(a) with the anomaly in Figure 13(b); the maximum amplitude of the anomaly is 0.032 s/km, which is about 10% of the local background slowness. Figure 14(a) shows the image of the 12 shot-gathers considered in the correct model; by comparing the correct image with the image obtained using the initial model (Figure 14(b)) we observe that several structural features are distorted and

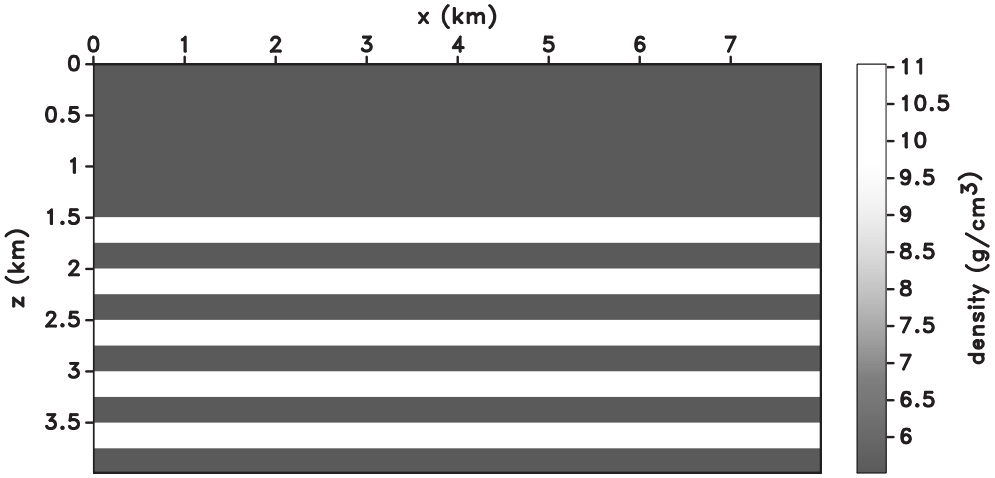

(a)

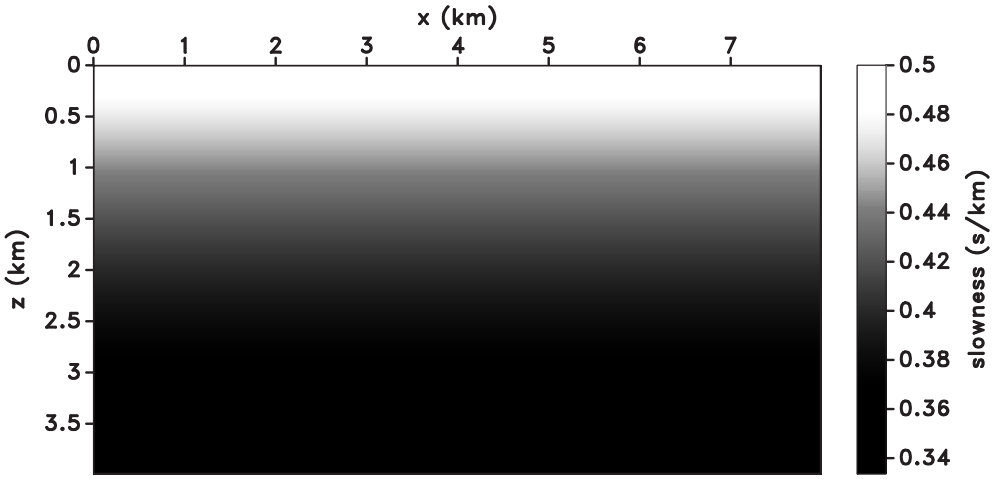

(b)

Figure 9. Model for the inversion test: (a) stack of layers with alternating values of density (b) correct slowness model.

the continuity of some reflectors broken (compare reflectors at lateral position $x = 2$ km). After 30 iterations of nonlinear conjugate-gradient we obtain the image in Figure 14(c): the bottom reflector is now more continuous and both the shape and amplitude of the dipping reflector in the middle section have been corrected; we want to highlight that, overall, we improved the image quality using a very limited number of shot-gathers. We also want to stress that these results do not involve any regularization or shaping of the estimated anomaly, which would greatly speed up convergence. Figure 15 shows the evolution of the objective function (the energy of the image perturbations) with the number of iterations; the objective function rapidly decreases to 50% of the initial value and then flattens. Since we use only a limited number of experiments (12), we introduce migration noise in the image, which prevents the inversion algorithm from further reducing the objective function. We want to emphasize, however, that we are able to correct the anomaly in the model using a small number of shots despite the lack of full illumination whereas methods based on focusing measures (i.e. migration velocity analysis based on extended images) need complete angular coverage to evaluate focusing in the image domain.

5 DISCUSSION

Our objective function measures the constructive interference of pairs of images using the warping field that relates them and the structural dip. The velocity error produces shifts of the image points, which can be observed in the image cube as moveout as a function of an extension parameter (e.g., the reflection angle or the shot index). The moveout represents a velocity error indicator and is inverted for updating the velocity model. In the literature (Biondi and Symes, 2004a; Sava and Fomel, 2006; Xie and Yang, 2008), the assumption of a shift along the normal to the reflector is commonly made; however,

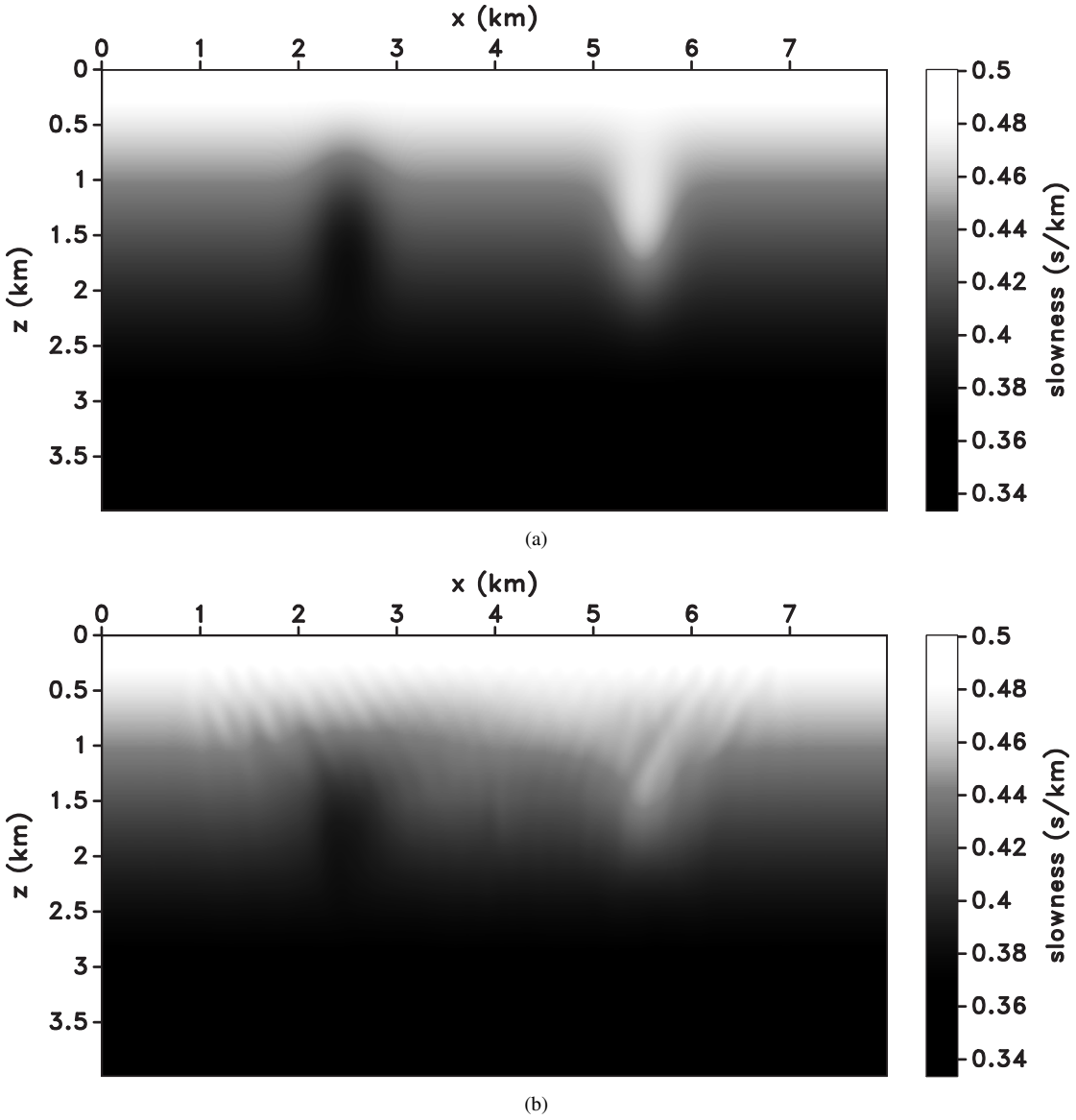

Figure 10. Slowness model: (a) initial and (b) updated.

as Xie and Yang (2008) point out, this is just an approximation in a general case of complex geology and velocity model. Moreover, the residual moveout is often measured along just the vertical direction, i.e., in CIGs, rather than along the normal to the reflector, and then converted into the normal residual moveout using simple trigonometry. That approach relies on the assumption that the dip of the reflector is independent of the velocity in the overburden. In general, this is not true. Our approach directly evaluates the degree of constructive interference of adjacent experiments and does not rely on any assumption about the direction of the shift of the image point in the migrated domain. Moreover, we are able to measure the 3D shift of the image point between the two experiments and then capture the complete kinematic information.

Operating in the image space, we can analyze all points in the portion of the model illuminated by the two experiments simultaneously and recover a spatially extended indicator of velocity error within the aperture of the experiments. This approach is computationally convenient because the construction of CIGs requires the subsampling of the image space for handling the dimensionality of the problem and the associated computational cost, whereas our method does not require gathers and supplies reliable information about the velocity inconsistencies in the area of the model illuminated by the seismic experiments.

Migration velocity analysis is based on kinematic assumptions: the correct velocity model returns a prestack image cube characterized by *horizontal* events along the exper-

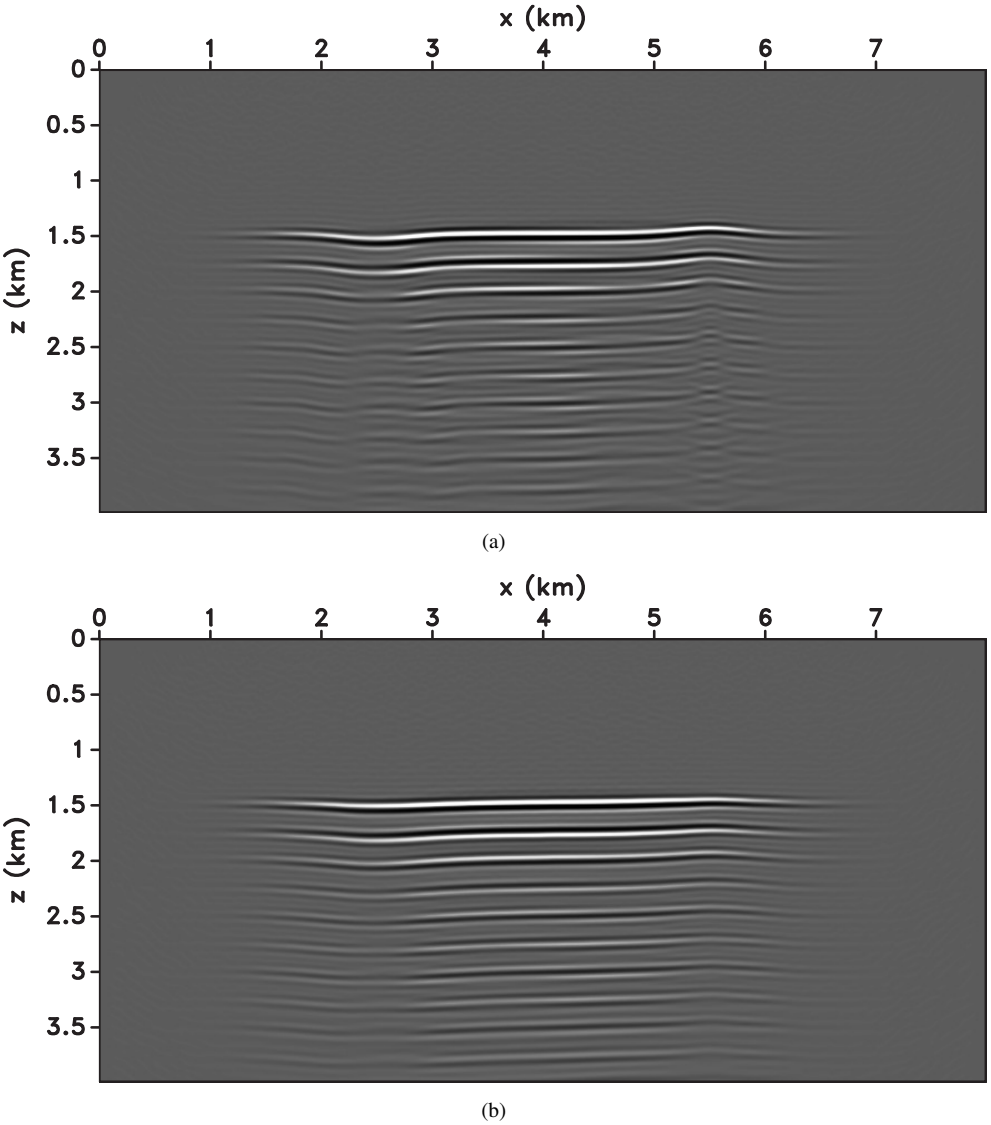

Figure 11. Migrated images: (a) image obtained with the initial velocity model and (b) after 10 velocity updates. The image in (b) is obtained after 10 nonlinear conjugate gradient iterations; every linearized problem involves five iterations of conjugate gradient. Note the better focusing of the image.

iment axis. Note that we say *horizontal* and not *constant in amplitude*, highlighting the kinematic nature of the conventional semblance principle. As already discussed by Mulder and Kroode (2002), the amplitudes of images from nearby experiments are likely to be similar but not equal. Reflection coefficients should be taken into account, and the velocity model itself, if it is highly heterogeneous, can lead to important differences in the amplitudes.

The image-domain implementation and the differential semblance approach makes our strategy (as opposed to WI) robust against local minima and cycle skipping; the measure of velocity error is independent of the migration algorithm and in principle either a one-way or a two-way velocity update engine can be used. The implementation of the WEMVA procedure, in contrast, relies on a one-way operator and cannot be directly extended to two-way operators.

The differential semblance approach makes both strategies discussed in this paper robust against cycle skipping. If the current velocity model is reasonably close to the true model, a cycle skip of the two images is unlikely. The chance of cycle skipping depends not only on the velocity model but also on other factors such as the shot positions and the frequency bandwidth of the signals. By increasing the distance between the shots, we violate the assumption of sharing the same aperture and the potential for cycle skipping grows. Increasing the bandwidth of the signals reduces the wavelength,

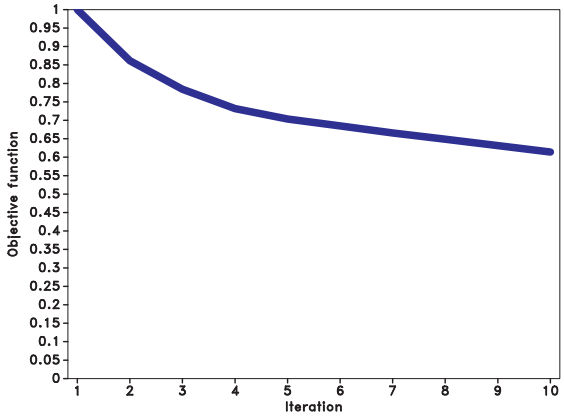

Figure 12. The decrease of objective function indicates that we are approaching the correct model.

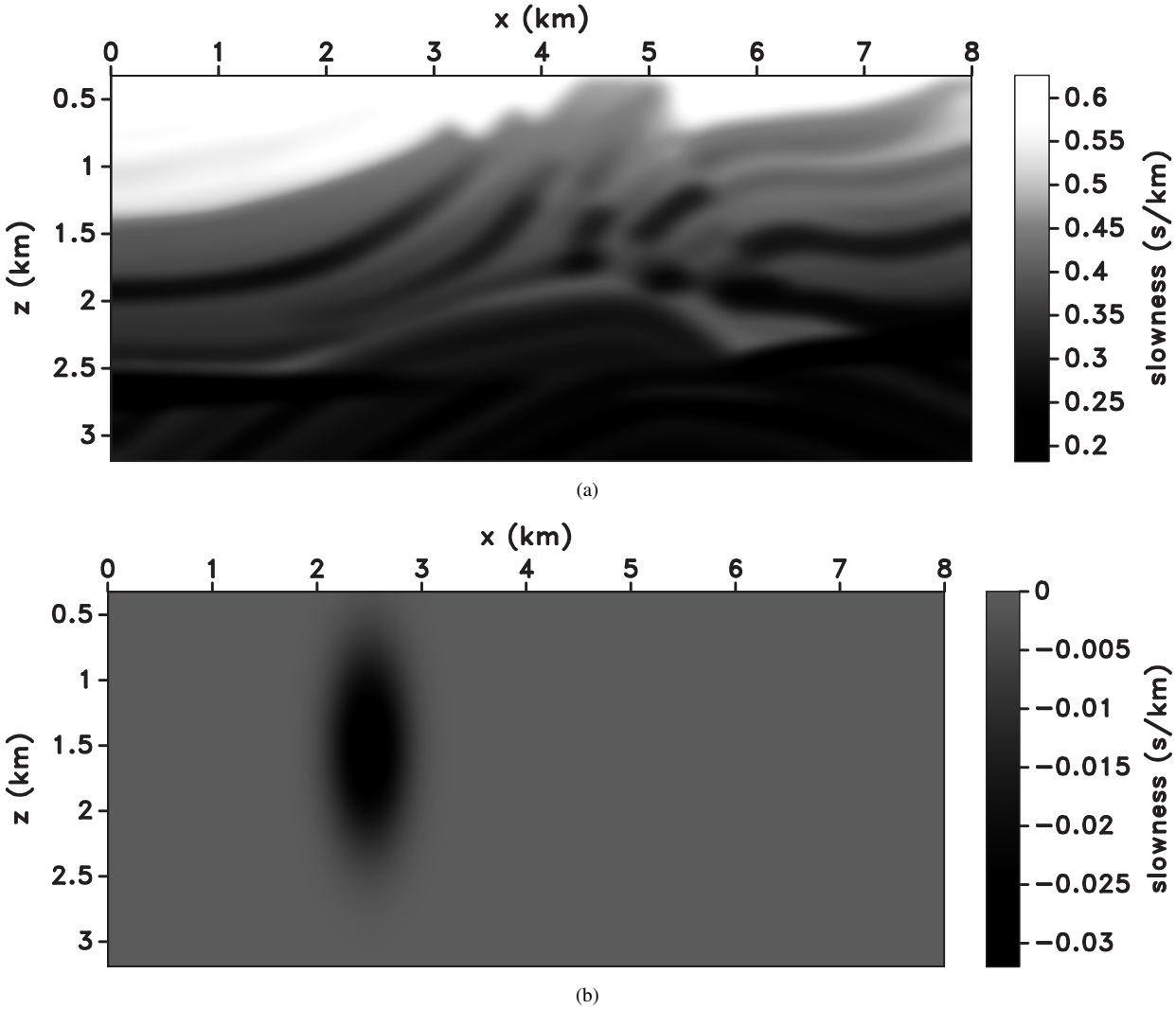

Figure 13. Macro slowness model (a) for the Marmousi dataset and (b) slowness perturbation for the model in (a).

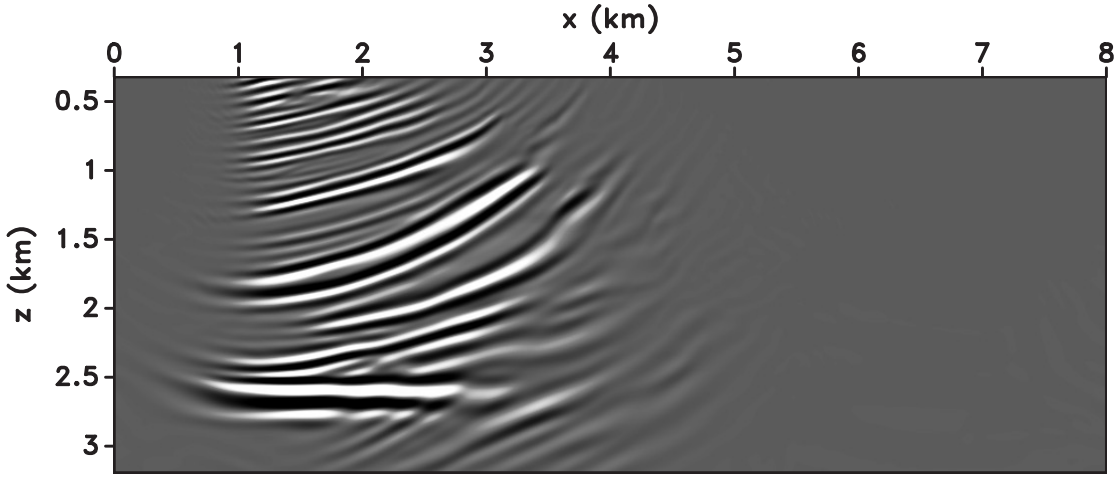

(a)

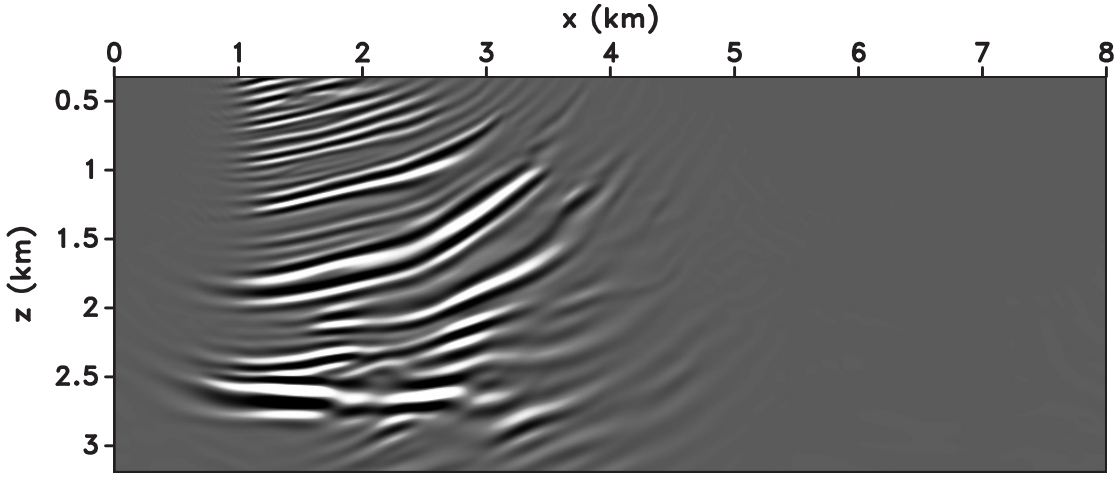

(b)

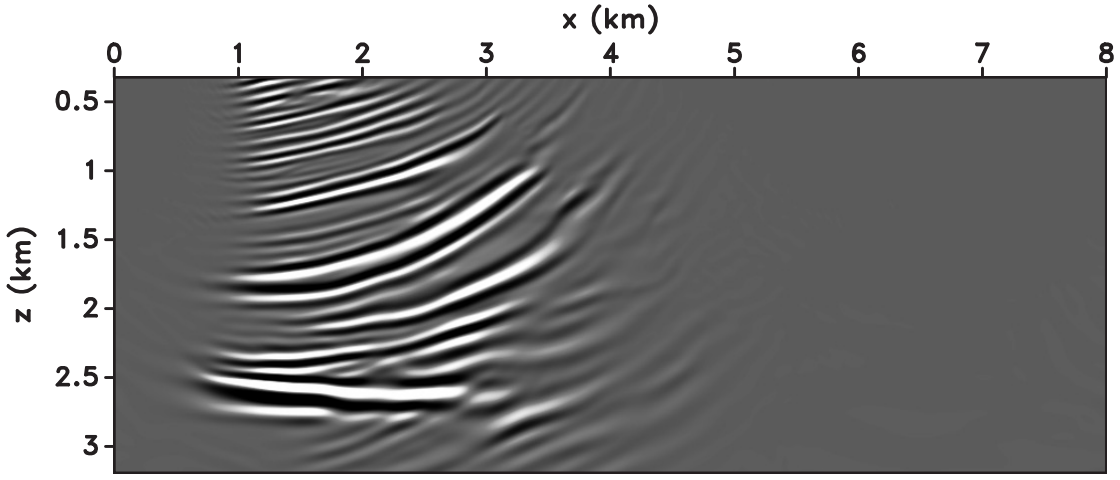

(c)

Figure 14. Image obtained using the correct slowness model (a), initial migrated image (b), migrated image after 30 iterations of nonlinear conjugate-gradient (c). We consider 12 shots, evenly spaced by 0.04 km at the surface; the first shot is positioned at $x = 0.96$ km. The receivers are are spaced 0.008 km on the surface and they are located at every grid point. Observe the improved continuity of the bottom reflector and the correction of the distortion of the middle dipping interfaces at a lateral position about $x = 2$ km.

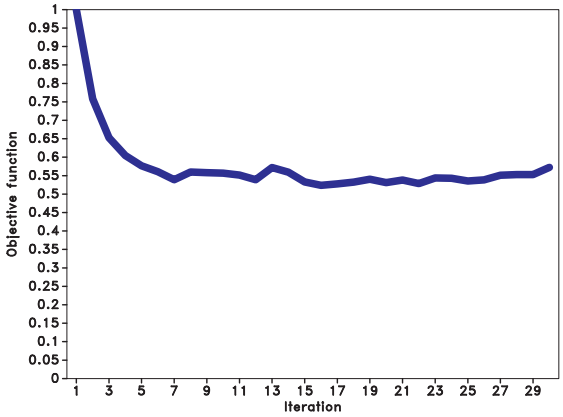

Figure 15. The objective function decreases rapidly and reaches a floor that depends on the limited number of sources we used in the inversion.

thus further constraining the maximum distance between adjacent experiments. For the image difference, the shot distance enhances the amplitude mismatch, thus the image perturbation can experience both cycle skipping and incomplete event cancellation, especially for strong and shallow reflectors. The construction of the image perturbation as the first order term of a Taylor series expansion removes the sensitivity to amplitude mismatching. Also cycle skipping is avoided since we are not computing differences but we construct the image perturbation from a single image and the estimated warping vector field.

Several critical points must be carefully handled. First, since we are using only pairs of experiments, the signal-to-noise ratio (SNR) can be low and the effectiveness of the algorithm may be hampered by the quality of the data. The sensitivity to the signal-to-noise ratio can be addressed using shot-encoding techniques (Whitmore, 1995; Zhang et al., 2005; Morton and Ober, 1998; Soubaras, 2006; Perrone and Sava, 2011) under the assumption that the different experiments are contaminated by uncorrelated noise. Second, because of cycle skipping between images, our approach can be ineffective if the shots are too far from each other, the velocity model is very inaccurate, or the reflector geometry is complex (e.g. around fault zones or in areas with conflicting dips). The similarity of nearby experiments is an assumption of every DSO-like optimization scheme; if the particular acquisition geometry or the complex wavepaths create shadow zones or illumination holes, DSO is likely to under perform. In the shot-domain, diving waves create images that do not correspond to reflection events and that do not satisfy the warping relationship assumed in this paper. Analogous considerations apply to multiply scattered wave and converted waves, which are not correctly handled by migration algorithms based on the Born approximation. Apparent reflectors associated with multiples and converted waves do not satisfy the warping relationship we assumed for the definition of the objective function and thus introduce a systematic bias in the inversion scheme.

6 CONCLUSIONS

We introduce a new measure of velocity errors for migration velocity analysis in the shot-domain. Our measure is based on the structural information in the image (the dip vector field) and a second vector field that links the images of adjacent experiments. This second vector field warps the first image into the second and captures the apparent displacement attributable to the shift in source position (in conventional shot-gather migration) or different ray-parameter (in plane-wave migration). The correct velocity model leads to images that build up along the reflectors; hence, by measuring the angle between the dip and the warping vector fields we can estimate velocity errors. Our criterion restates the semblance principle and takes into account the motion of the image points as a function of shot position and velocity model, instead of considering gathers and moveout in the vertical direction only. The method allows one to assess the correctness of the velocity model at every point in the image space within the aperture of the two considered shots; moreover, since no gather is required, one can bootstrap the velocity-analysis step while imaging. Possible downsides are related to reduced the signal-to-noise ratio, which is smaller because we consider groups of experiments at a time instead of the entire dataset. The formulation of the optimization problem for the velocity model naturally leads to an expression for an image perturbation for wave-equation migration velocity analysis. The image perturbation is computed as the inner product between the image gradient and the warping vector field at every image point, i.e., the first-order term of a pointwise Taylor series expansion based on the warping relationship between the two images. If the velocity model is correct, the image gradient (orthogonal to the structure) and the displacement field (parallel to the structure) are orthogonal, the objective function is minimum, and the image perturbation is zero. A synthetic test involving local velocity anomalies and severe focusing and defocusing of the wavefields show the effectiveness of our approach for linearized migration velocity analysis.

7 ACKNOWLEDGMENT

We would like to acknowledge the financial support provided by a research grant from eni E&P. The reproducible numeric examples in this paper use the Madagascar open-source software package (http://www.reproducibility.org). We thank Jeff Godwin for integrating the Mines JTK (http://inside.mines.edu/∼dhale/jtk/) and the Madagascar.

REFERENCES

Aki, K., and P. G. Richards, 2002, Quantitative seismology, second edition ed.: University Science Books.

Al-Yahya, K., 1989, Velocity analysis by iterative profile migration: Geophysics, **54**, P. 718–729.

Biondi, B., and P. Sava, 1999, Wave-equation migration velocity analysis: Presented at the 69th Ann. Internat. Mtg., SEG.

Biondi, B., and W. Symes, 2004a, Angle-domain common-image gathers for migration velocity analysis by wavefield-continuation imaging: Geophysics, **69**, 1283–1298.

Biondi, B., and W. W. Symes, 2004b, Angle-domain common-image gathers for migration velocity analysis by wavefield continuation imaging: Geophysics, **69**, 1283–1298.

Chavent, G., and C. A. Jacewitz, 1995, Determination of background velocities by multiple migration fitting: Geophysics, **60**, 476–490.

de Vries, D., and A. J. Berkhout, 1984, Velocity analysis based on minimum entropy: Geophysics, **49**, 2132–2142.

Fei, W., and P. Williamson, 2010, On the gradient artifacts in migration velocity analysis based on differential semblance optimization: Presented at the 80th Ann. Internat. Mtg., Soc. of Expl. Geophys.

Fomel, S., 2002, Applications of plane-wave destruction filters: Geophysics, **67**, 1946–1960.

Hale, D., 2007a, Local dip filtering with directional laplacian: Technical Report CWP-567, Center for Wave Phenomena, Colorado School of Mines.

———, 2007b, A method for estimating apparent displacement vectors from time-lapse seismic data: Technical Report CWP-566, Center for Wave Phenomena, Colorado School of Mines.

Morton, S. A., and C. C. Ober, 1998, Faster shot-record migration using phase encoding: Presented at the 68th Ann. Internat. Mtg., SEG.

Mulder, W. A., and A. P. E. Kroode, 2002, Automatic velocity analysis by differential semblance optimization: Geophysics, **67**, 1184 – 1191.

Perrone, F., and P. Sava, 2011, Wave-equation migration with dithered plane waves: Geophysical Prospecting.

Plessix, R.-E., 2009, Three-dimensional frequency-domain full-waveform inversion with an iterative solver: Geophysics, **74**, WCC53–WCC61.

Pratt, R. G., 1999, Seismic waveform inversion in the frequency domain, part 1: Theory and verification in a physical scale model: Geophysics, **64**, 888–901.

Rickett, J., and P. Sava, 2002, Offset and angle-domain common image-point gathers for shot-profile migration: Geophysics, **67**, 883–889.

Sava, P., and B. Biondi, 2004, Wave-equation migration velocity analysis. i. theory: Geophysical Prospecting, **52**, 593–606.

Sava, P., and S. Fomel, 2003, Angle-domain common image gathers by wavefield continuation methods: Geophysics, **68**, 1065–1074.

———, 2006, Time-shift imaging condition in seismic migration: Geophysics, **71**, S209–S217.

Sava, P., and I. Vlad, 2008, Numerical implementation of wave-equation migration velocity analysis operators: Geophysics, **73**, VE145–VE159.

Shen, P., and W. W. Symes, 2008, Automatic velocity analysis via shot profile migration: Geophysics, **73**, VE49–VE59.

Soubaras, R., 2006, Modulated-shot migration: 76th Ann. Internat. Mtg., Soc. of Expl. Geophys., 2430–2433.

Soubaras, R., and B. Gratacos, 2007, Velocity model building by semblance maximization of modulated-shot gathers: Geophysics, **72**, U67–U73.

Stoffa, P. L., J. T. Fokkema, R. M. de Luna Freire, and W. P. Kessiger, 1990, Split-step fourier migration: Geophysics, **55**.

Symes, W. W., 2008, Migration velocity analysis and waveform inversion: Geophysical Prospecting, **56**, 765–790.

Symes, W. W., and J. J. Carazzone, 1991, Velocity inversion by differential semblance optimization: Geophysics, **56**, 654–663.

Taner, M. T., and F. Koehler, 1969, Velocity spectra - digital computer derivation and applications of velocity functions: Geophysics, **34**, 859 – 881.

Tarantola, A., 1984, Inversion of seismic reflection data in the acoustic approximation: Geophysics, **49**, 71–92.

van Vliet, L. J., and P. W. Verbeek, 1995, Estimators for orientation and anisotropy in digitalized images: Proceedings of the first annual conference of the Advanced School for Computing and Imaging, ASCI'95, 442–450.

Vasconcelos, I., 2008, Generalized representations of perturbed fields - applications in seismic interferometry and migration: 77th Annual International Meeting, SEG, Expanded Abstracts, 2927–2931.

Vogel, C., 2002, Computational methods for inverse problems: SIAM.

Whitmore, N., 1995, An imaging hierarchy for common-angle plane wave seismograms: PhD thesis, University of Tulsa.

Woodward, M. J., 1992, Wave-equation tomography: Geophysics, **57**, 15–26.

Xie, X. B., and H. Yang, 2008, The finite-frequency sensitivity kernel for migration residual moveout and its applications in migration velocity analysis: Geophysics, **73**, S241–S249.

Yilmaz, O., 2001, Seismic data processing: SEG.

Zhang, Y., J. Sun, C.Notfors, S. H. Gray, L. Chernis, and J. Young, 2005, Delayed-shot 3d depth migration: Geophysics, **70**, E21–E28.